Temperature-induced and electric-field-induced phase transitions in rhombohedral $Pb(In_{1/2}Nb_{1/2})O_3$-$Pb(Mg_{1/3}Nb_{2/3})O_3$-$PbTiO_3$ ternary single crystals

Yaojin Wang (汪尧进),* Zhiguang Wang, Wenwei Ge, Chengtao Luo, Jiefang Li, and D. Viehland
Materials Science and Engineering, Virginia Tech, Blacksburg, Virginia 24061, USA

Jianwei Chen and Haosu Luo
Shanghai Institute of Ceramics, Chinese Academy of Sciences, 215 Chengbei Road, Jiading, Shanghai 201800, China
(Received 16 January 2014; revised manuscript received 3 October 2014; published 23 October 2014; corrected 30 October 2014)

Temperature and electric field effects on rhombohedral (R) ternary $Pb(In_{1/2}Nb_{1/2})O_3$-$Pb(Mg_{1/3}Nb_{2/3})O_3$-$PbTiO_3$ (PIN-PMN-PT) ferroelectric single crystals were comprehensively studied by x-ray diffraction. We have focused on how the individual phase transitions as well as the phase transition sequences depend on thermal and electrical history. Electric field-temperature phase diagrams have been constructed under [001] field-cooling and field-heating conditions. As happens to the R phase of binary PMN-PT crystals [H. Cao, J. F. Li, D. Viehland, and G. Y. Xu, Phys. Rev. B **73**, 184110 (2006)], the R phase of the zero-field-cooled (ZFC) state is replaced by a monoclinic A (M_A) phase in the field-cooled (FC) diagram. In particular, reciprocal-space mesh scans demonstrated that the M_A phase was stable for crystals poled along the [001] crystallographic direction rather than the initial R phase of the ZFC state. Furthermore, an E-field-induced phase transformational sequence of $R \rightarrow M_A \rightarrow$ tetragonal (T) was observed at constant temperature, revealing a gradual increase in the c lattice parameter. These findings demonstrate that the ternary PIN-PMN-PT crystals exhibit common phase transition features with binary PMN-PT and $Pb(Zn_{1/3}Nb_{2/3})O_3$-$PbTiO_3$ (PZN-PT) ones for compositions in the low PT side of the morphotropic phase boundary.

DOI: 10.1103/PhysRevB.90.134107 PACS number(s): 77.84.Bw, 77.80.bg, 77.80.Jk, 61.05.F−

I. INTRODUCTION

Perovskite oxides have attracted increasing interest over the past decades from the viewpoint of their excellent ferroelectric and piezoelectric properties for applications in multifunctional devices (such as sensors, transducers, actuators, and memory devices), as well as for an understanding of the fundmental physics underlying their high properties [1]. Among these materials, lead-based solid solutions of $Pb(Zn_{1/3}Nb_{2/3})O_3$-$PbTiO_3$ (PZN-PT) and $Pb(Mg_{1/3}Nb_{2/3})O_3$-$PbTiO_3$ (PMN-PT) with an ultrahigh electromechanical response that is nearly an order of magnitude larger than those of conventional piezoelectric ceramics [2] have been extensitively investigated, especially for compositions near a mophotronic phase boundary (MPB) [3].

An important breakthrough in understanding the strucural origin of the high electromechanical properties was the experimental discovery and subsequent theoretical study of low-symmetry ferroelectric monoclinic phases that bridge the high-symmetry rhombohedral (R, space group $R3m$) and tetragonal (T, space group $P4mm$) ones [4–7]. Controversy remains concerning whether these monoclinc phases are intrinsic homogeneous phases or rather structurally heterogeonous ones [8,9]. Either way, the monoclinic symmetry allows the polarization vector to be unconstrained within a plane rather than being confined to a particular crystallographic axis. The monoclinic A (M_A) unit cell is doubled in volume and rotated by 45° about the c axis with respect to the pseudocubic cell, having a unique b_{Ma} axis along the [110] direction, whereas the monoclinic C (M_C) unit cell is primitive, having a unique b_{Mc} axis that is oriented along the pseudocubic [010], as illustrated in Fig. 1(a). More recently, a monoclinic B (M_B) phase has been reported [10–12]. Although both the M_A and M_B phases belong to the Cm space group, the difference between them lies in the magnitudes of the components of the polarization corresponding to the pseudocubic cell: for the M_A phase, $P_x = P_y < P_z$, whereas for the M_B phase, $P_x = P_y > P_z$ [7]. Comparing the relative values of P_x, P_y, and P_z is not always straightforward by structural measurements. However, Cao *et al.* [11] proposed a criterion to experimentally distinguish the M_A and M_B phases based on the values of their lattice parameters.

Monoclinic M_A, M_B, and M_C phases have all been reported in both PZN-PT and PMN-PT crystals. Neutron and x-ray diffraction studies of the effect of an electric field E on [001]-oriented rhombohedral PZN-4.5PT and PMN-28PT (both on the low PT side of the MPB) have shown a cubic (C)$\rightarrow T \rightarrow M_C$ transformational sequence on being field-cooled (FC) [11] and a $R \rightarrow M_A \rightarrow T$ transformation sequence with increasing E applied along the [001] at fixed temperature [13,14]. More complicated transformational sequences have been observed for compositions near the MPB [2,15]. For example, the initial R phase of PZN-8PT and PMN-30PT is irreversibly transformed to a T one via both M_A and M_C phases under E//[001] [13–16]. In these cases, polarization rotation within two monoclinic planes and a jump between them occurs with increasing E, as shown in Fig. 1(b). Accordingly, a phase transformational sequence of $C \rightarrow T \rightarrow M_C$ [15] or $C \rightarrow T \rightarrow M_C \rightarrow M_A$ [10,16] was obtained in the FC condition. In particular, the M_C phase of PZN-8PT and the M_A one of PZN-4.5PT and PMN-30PT remained after application of E. Previous investigations have also revealed that E applied along other crystallographic directions leads to different polarization rotation pathways and phase transformational sequences [11,17]. In PMN-30PT crystals, for

*Email address: yaojin@vt.edu

 ©2014 American Physical Society

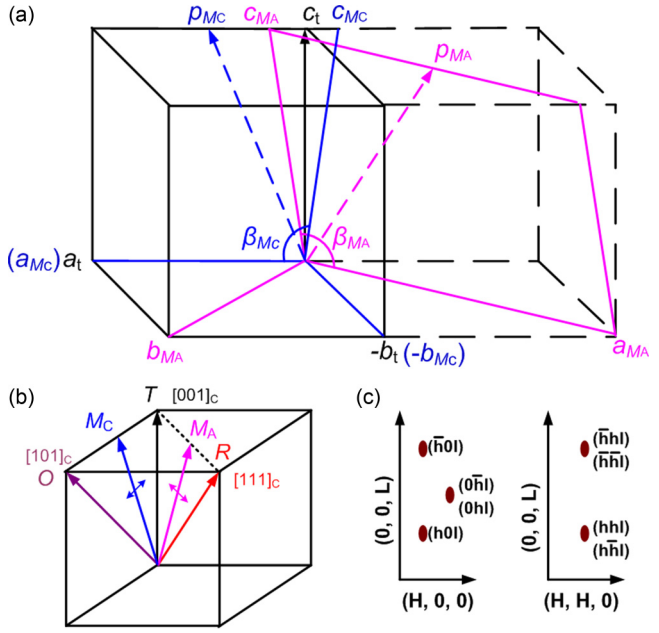

FIG. 1. (Color online) (a) Representation of the monoclinic unit cell with respect to the tetragonal unit cell, adapted from Ref. [3]. The polarization in monoclinic M_A (space group Cm) lies in the $a_{MA}c_{MA}$ monoclinic plane (polarization $P = [xxz]$ in cubic Cartesian coordinates) and is shown as p_{MA}; the polarization in monoclinic M_C (space group Pm) lies in the $a_{MC}c_{MC}$ plane (polarization $P = [x0z]$) and is shown as p_{MC}. (b) Scheme of two possible paths ($R \rightarrow M_A \rightarrow T$ and $R \rightarrow M_A \rightarrow M_C \rightarrow T$) for the polarization vectors to change from [111] in the rhombohedral phase to [001] in the tetragonal one, as proposed by Fu and Cohen [5]. (c) Schematic representation of reciprocal-space maps of a monoclinic structure, indexed in the monoclinic system.

$E//[101]_C$, a $R \rightarrow M_B \rightarrow$orthorhombic ($O$) transformational sequence has been found [10,18], which had anhysteretic electromechanical behavior [19] and a monodomain O phase under high field [20]. Diffraction studies have shown that the M_B phase is the ground-state condition upon removal of $E//[110]$ [10]. Electric field versus temperature (E-T) phase diagrams in the FC state or at fixed temperatures with increasing E and temperature versus PT composition ones in the FC state have been constructed based on these structural studies [10,11,13,15,16].

In spite of the extraordinary electromechanical properties of PMN-PT and PZN-PT crystals, several obstacles have restricted them from practical applications. First, deterioration in performance with increasing temperature limits their usable temperature ranges, which arises from a loss of the piezoelectric properties because of depolarization due to their relative low $M \rightarrow T$ and $T \rightarrow C$ transition temperatures. Second, the coercive field is on the order of 2 kV/cm, which restricts their usage to low voltage drive applications [21]. In order to overcome these challenges, numerous efforts have been carried out in an attempt to broaden the usable temperature and voltage ranges, generally by selecting solution components and dopants for the binary systems, such as $Pb(Yb_{1/2}Nb_{1/2})O_3$ (or PYN), $Pb(In_{1/2}Nb_{1/2})O_3$ (or PIN), and Mn [21,22].

Recently, high-quality and large size ternary PIN-PMN-PT crystals have been grown by a modified Bridgman method. These ternary crystals have Curie temperatures on the order of $T_C = 200\,°C$ while maintaining the ultrahigh piezoelectric properties of the binary PZN-PT and PMN-PT systems [21,23–25]. In these ternary crystals, the superior piezoelectric properties have been well characterized [21,24–30]. Furthermore, various phase transformation sequences have been conjectured to explain polarization, electromechanical, and dielectric data [26–28,30,31], and polarized light microscopy images [32]. However, to clarify the origin of the exceptional piezoelectric characteristics of this new generation of ternary crystals, high resolution diffraction studies are needed in order to resolve the complexities of the transformation sequences in detail.

Here, high resolution x-ray diffraction structural investigations of PIN-PMN-PT crystals on the R side of the MPB have been performed for various electrical and thermal histories. Systematic studies have been carried out by (i) heating the crystals from 30 to 250 °C under $E = 0$ kV/cm (i.e., zero-field heated [ZFH]) and with $E//[001]$ (i.e., field heated [FH]), starting from the annealed state (annealing at 500 °C for 30 min in order to eliminate the pre-stress effect generated in the growth process); (ii) cooling from 250 to 30 °C with $E =$ 0 kV/cm [i.e., zero-field cooled (ZFC)] and with $E//[001]$ direction (i.e., FC); (iii) heating the poled crystal from 30 to 250 °C [i.e., poled-heating (PH), the poled state was achieved via poling the sample using $E = 8$ kV/cm along [001] direction at room temperature]; and (iv) increasing E at constant temperatures. The results unambiguously identify the E-T phase diagram and the transformational sequences for these different electrical and thermal histories of ternary PIN-PMN-PT crystals.

II. EXPERIMENTAL DETAILS

Ternary single crystals with the nominal composition of 33PIN-35PMN-32PT were grown from the melt by a modified Bridgman method [25]. As-grown single crystals were oriented along pseudocubic (100)/(010)/(001) planes, diced into parallelepipeds with dimensions of $4 \times 3 \times 3\,mm^3$ from the rhombohedral region [23,25], and all the faces of the parallelepipeds were polished to 0.25 μm. The actual composition for these crystals was determined to be 25PIN-42PMN-33PT using energy dispersive x-ray spectroscopy (EDS; experimental error ~5%). In order to avoid experimental errors due to segregation (composition gradient from top to bottom of the as-grown crystals [23,25]), the rectangular parallelepipeds were diced into two pieces of dimensions $3 \times 3 \times 0.5$ and $3 \times 3 \times 3\,mm^3$ (the larger crystal was intended to be a backup in case of dielectric breakdown during measurements under E). The cut faces were reoriented/polished along the (001) crystallographic planes to a roughness of 0.25 μm using a polishing grinder. All the measurements reported here were performed on the same crystal of dimensions $3 \times 3 \times 0.5\,mm^3$.

The temperature-dependent dielectric constant was characterized using an LCR meter (HP 4284A) at various fields and temperatures, which will be described in more detail with regard to diffraction measurements. The x-ray diffraction

studies were performed using a Philips MPD high-resolution system equipped with a two-bounce hybrid monochromator, an open three-circle Eulerian cradle, and a domed hot stage. A Ge (220)-cut crystal was used as an analyzer, which provides an angular resolution of 0.0068° [full width at half-maximum (FWHM)]. The experimental error in lattice parameters in this investigation was determined to be less than 0.002 Å, via cross-checking the diffraction peaks along $(002)_C$ and $(200)_C$ or $(220)_C$ zones. The x-ray wavelength was that of Cu $K\alpha$ = 1.5406 Å, and the x-ray generator was operated at 45 kV and 40 mA. Previous x-ray and neutron scattering studies revealed the presence of a strong "skin effect" [33] in single crystal relaxor compositions of both PZN-PT [34,35] and PMN-PT [36,37] that can produce variability in the diffraction peaks profiles and lattice parameters. The thickness of this skin seems to be system dependent, but it is of order 60 μm in pure PZN. Given that this skin effect may be present in PIN-PMN-PT, we note that the x-ray penetration depth in our measurements was approximately 10 μm [10,11].

Gold electrodes were deposited on the top and bottom surfaces of the specimen (i.e., 3×3 mm^2) by sputtering. Diffraction measurements were then performed along the (00L) direction (i.e., x-ray beam on top and bottom faces); we designate, here, the electroded faces as (001). Upon finishing the measurements along (001), the electrodes were removed using a polishing blanket with 0.25 μm aluminum powder. Then, the specimen was re-electroded on one pair of side faces perpendicular to the original (001) by sputtering (i.e., 3×0.5 mm^2). Thereafter, diffraction measurements were carried out along (H00) and (HH0) zones. Studies were performed under electric field by attaching thin wires on the electroded faces using a small drop of conducting epoxy, and silicon grease with high dielectric breakdown strength was used to prevent arcing. To determine the domain configuration, reciprocal-space mesh scans (RMS) were obtained around the (200) Bragg diffractions in the (H, 0, L) zone and around (220) in the (H, H, L) zone. These RMS were recorded by a sequence of 2θ-ω scans at different ω offsets and are shown in plots of intensity as a function of reciprocal lattice units (rlu). In this study, we fixed the value of rlu at $a^* = 2\pi/a = 1.550$ Å^{-1}, and all RMS of PIN-PMN-PT shown here were plotted in reference to this reciprocal unit. For both the ZFC and FC states, the specimen was heated to 250 °C, and measurements were subsequently taken on cooling without and with E, respectively. In both the ZFH and FH measurements, each measurement cycle was begun by heating the crystal to 250 °C in order to completely anneal the crystal specimen and cooled down to 30 °C, and measurements subsequently taken on heating without and with E, respectively. In the PH measurements, the specimen was poled at room temperature directly from the annealed state under E = 8 kV/cm and then gradually heated to 250 °C. In the increasing field at fixed temperature measurements, the specimen was heated to 60 and 100 °C from an initially annealed state, and measurements subsequently performed with first increasing and then decreasing E. The heating and cooling rates were 2 °C/min for temperature-dependent dielectric constant and 5 °C/min for the x-ray measurements.

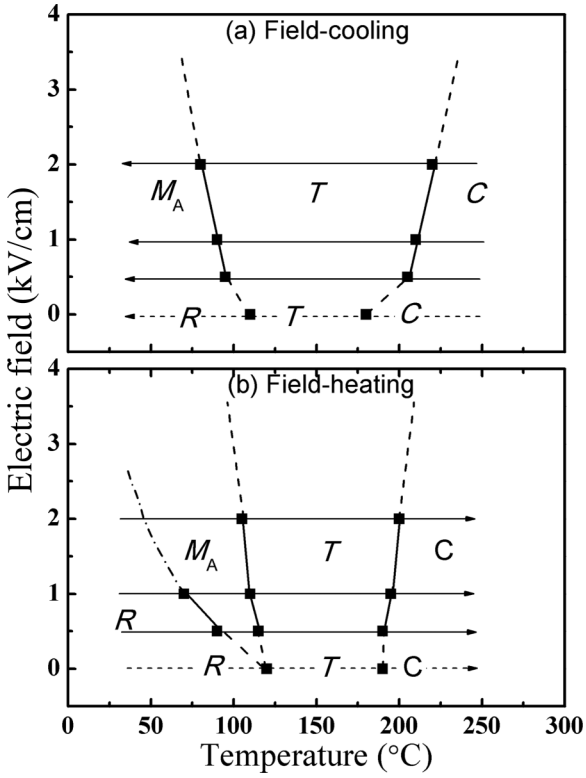

FIG. 2. Field-temperature phase diagram of rhombohedral PIN-PMN-PT, respectively obtained from structural measurement in the (a) FC process and (b) FH process with E = 1 kV/cm. The phase transition under ZFC and ZFH was also present in this figure, labeled with dashed arrows.

III. PHASE TRANSITIONS AND LATTICE PARAMETERS

First, we show an E-T phase diagram for PIN-PMN-PT in Fig. 2, which summarizes the findings of the measurements to be presented in the following sections. The top panel of this figure gives the FC diagram, where measurements were made under a constant field on cooling from 250 to 30 °C; the bottom panel shows the FH diagram, where measurements were performed under a constant field on heating from 30 to 250 °C beginning from an initially ZFC condition. To present a more comprehensive perspective, the initial ZFC and ZFH conditions (E = 0 kV/cm) are also presented in these diagrams. Solid squares represent the phase transition temperatures, which were determined by changes of the lattice constants and peak profiles. The significant features that can be seen in the field-temperature phase diagrams with increasing E are as follows: (i) the $C \rightarrow T$ boundary shifts to higher temperature and (ii) the $T \rightarrow M_A$ boundary shifts slightly to lower temperature. These features demonstrate that the T phase is stabilized with increasing E [11,15,16]. In this diagram, arrows are used to indicate the measurement direction and range with corresponding temperature changes.

A. Dielectric-temperature response

Figure 3(a) shows the temperature-dependent 1 kHz dielectric constant ε_r for PIN-PMN-PT crystals measured under various conditions, as described in Sec. II. The dielectric

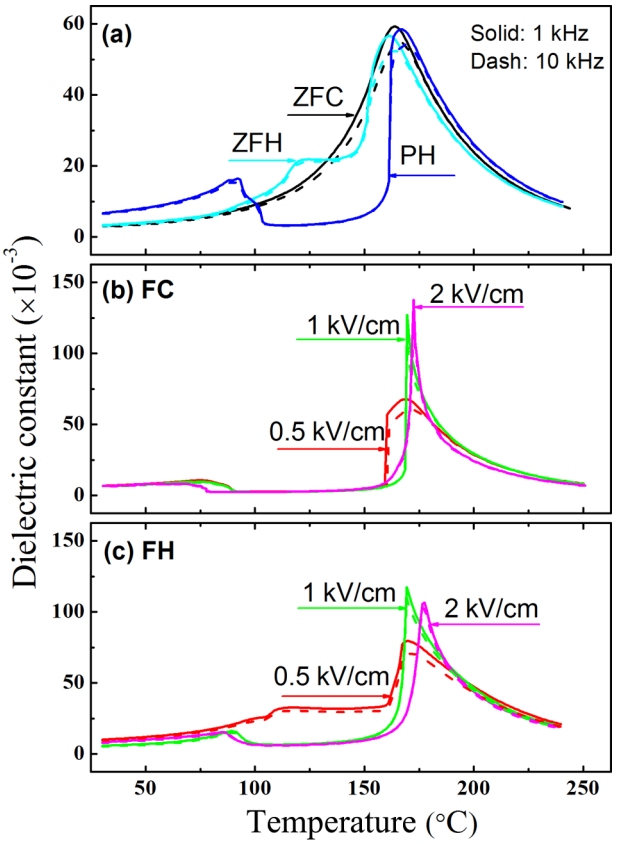

FIG. 3. (Color online) Temperature dependence of the dielectric constant at 1 kHz (solid lines) and 10 kHz (dash lines): (a) for ZFC, ZFH, and PH processes; (b) under various E fields of $E = 0.5$, 1, and 2 kV/cm for FC process; (c) under various E fields of $E = 0.5$, 1, and 2 kV/cm for FH process.

response for the ZFC condition exhibits a single, broad, and featureless peak that is typical of a diffuse phase transition, whereas, an additional dielectric shoulder is observed under the ZFH and PH conditions. In the case of pure PMN, Westphal *et al.* [38] reported dielectric and optical birefringence data that suggest cubic and ferroelectric phases coexist over a broad temperature range and that the relative volume fraction of these phases changes with temperature. We observe similar behavior in PIN-PMN-PT using x-ray diffraction measurements, which will be discussed in more detail later. In the FC condition for $E = 0.5$ kV/cm [see Fig. 3(b)], a broad dielectric maximum is found typical of a diffuse phase transformation, followed by a sharp drop in the dielectric constant near 160 °C. We believe this sharp decrease represents a pseudocubic (relaxor)$\rightarrow T$ transition, which is supported by the x-ray data to be presented. At higher field strengths of $E = 1$ and 2 kV/cm, two dielectric peaks were apparent. The first is associated with a sharp $C \rightarrow T$ transition followed by an abrupt decrease in the dielectric constant: these data indicate that the dielectric maximum and relaxor$\rightarrow T$ transition coincide. The second is a dielectric shoulder at lower temperatures that indicates a ferroelectric phase transition. For the FH condition [see Fig. 3(c)], in addition to these two dielectric peaks, a weaker third peak in the dielectric data is observed for $E = 0.5$ kV/cm, which is attributed to a $R \rightarrow M_A$ transition.

An important observation from these data is the apparent increase of the dielectric maximum (i.e., $C \rightarrow T$) phase transition temperature (or T_C) with increase of E in both the FC and FH conditions, which is consistent with that previously reported in binary PMN-PT and PZN-PT crystals [15,16,39]. In addition, the dielectric maximum becomes noticeably sharper for $E \geq 1$ kV/cm. We speculate that these characteristics may be universal to Pb-based piezoelectric crystals near the MPB. A possible explanation of these two characteristics is that polar nanodomains (PNDs) exist near T_C in the ZFC and ZFH conditions for compositions on the low-PT side of the MPB [39,40]. Application of E//[001] might align the PNDs and induce a macrodomain state. The observed shift in the $C \rightarrow T$ boundary may reflect this field-induced PNDs $\rightarrow$ macro T domains transition.

B. ZFC and ZFH x-ray data

Diffraction profiles measured along the radial (θ-2θ) direction in the pseudocubic (002) and (220) zones in the ZFC and ZFH conditions are shown in Fig. 4, where the Gaussian function fits are superposed on the observed diffraction peaks (in panels (a) and (b), the diffraction peaks at 140 °C were fitted using a Lorentzian function). In the ZFC condition, the C phase is stable above 190 °C, as only a single sharp peak is observed in the $(002)_C$ and $(220)_C$ diffractions. However, a broad tail at the low 2θ side (i.e., an asymmetrical profile) is observed above this temperature, as shown in Fig. 4 at 250 °C for both ZFC and ZFH conditions. In particular, above the Burns temperature (500 °C, data not shown), the tail behavior disappeared. This indicates that the tails are probably associated with short-range order [i.e., polar nanoregions (PNRs)], resulting from random electric field [41], as the B-site of PMN-PT type perovskites are occupied by near-random mixtures of heterovalent cations [42]. Another possible explanation for these tail features is the skin effect due to the limit penetration of x ray. On cooling to 180 °C, a $C \rightarrow T$ transition occurs and a tetragonal distortion of the (002) Bragg peak becomes apparent via the appearance of an additional peak at lower scattering angle. A coexistence of C and T phases is observed on cooling to 140 °C, where the pseudocubic (002) diffraction consists of a tetragonal (002)-(200) doublet and a residual cubic (002) singlet. When the temperature was lowered below 110 °C, a broad rhombohedral (002) singlet and a $(220) - (\bar{2}20)$ doublet are respectively observed in the pseudocubic (002) and (220) zones. This demonstrates that the R phase is stable on cooling. In the ZFH condition, a $R \rightarrow T$ transition was clearly identified at 130 °C, although some residual diffuse scattering in the vicinity of the rhombohedral (200) persisted. On further heating to 190 °C, a subsequent $T \rightarrow C$ transition is found, as evidenced by the appearance of cubic (002) and (220) diffractions and a simultaneous disappearance of the tetragonal a domain (200) peak.

The phase transition sequences in Fig. 2 under ZFC and ZFH were identified by the evolution of the diffraction peaks, as discussed above. In order to quantitatively determine the phase transition temperatures and to cross-check whether the polar state has long- or short-range order, the fitted FWHM of each peak along $(002)_C$ zone is given in Fig. 5. Obviously, the diffraction peaks of the polar state are much wider than those

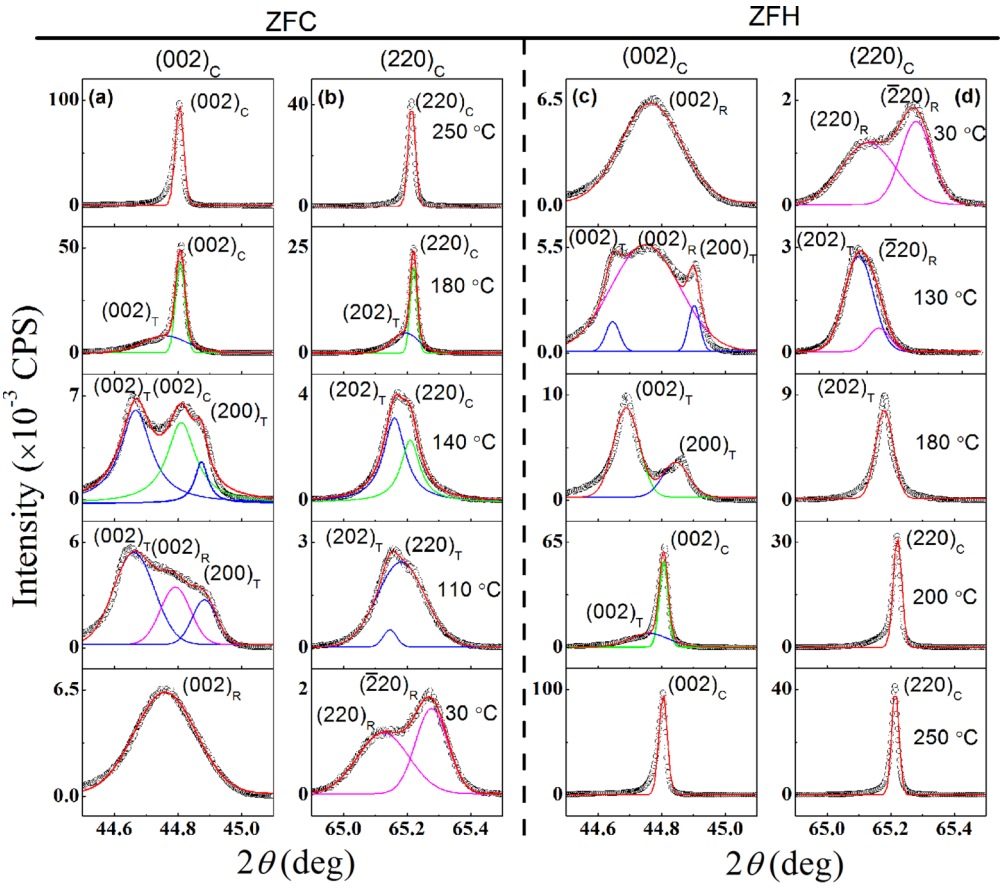

FIG. 4. (Color online) Temperature evolution of the (a) $(002)_C$ and (b) $(220)_C$ reflection peaks for ZFC from cubic to rhombohedral phase and (c) $(002)_C$ and (d) $(220)_C$ reflection peaks for ZFH from rhombohedral to cubic phase.

of the nonpolar cubic phase. For the T phase, the values of FWHM for the c domain peaks are larger than that for the a domain in both ZFH and ZFC conditions. In particular, the a domain of T phase exhibits similar FWHM values as the nonpolar cubic phase. We note that the large values of FWHM for the T c domain might be associated with the short-range T order; however, the peak characteristic for both the ZFC and ZFH conditions (i.e., the ZFC value of FWHM for the c domain increases with decreasing temperature, whereas it decreases with increasing temperature for ZFH) make this conjecture controversial. Analogously, in the low temperature range of both the ZFC and ZFH conditions, the large FWHM values of the $(002)_R$ diffraction peaks may also indicate a short-range rhombohedral ordering, or pseodu-R phase, as recently defined by Gehring *et al.* [42]. Please note that these broad features have previously been observed in binary PMN-PT relaxor crystals [16]. Thus, the polar T and R in the phases diagram of Fig. 2 and the phase coexistence regions in Figs. 6 and 7 can be regarded as long-range ordered states based on the general characteristics of their diffraction peaks, even though controversy remains. We hope our results will stimulate further neutron diffuse scatting experiment to clarify this controversy.

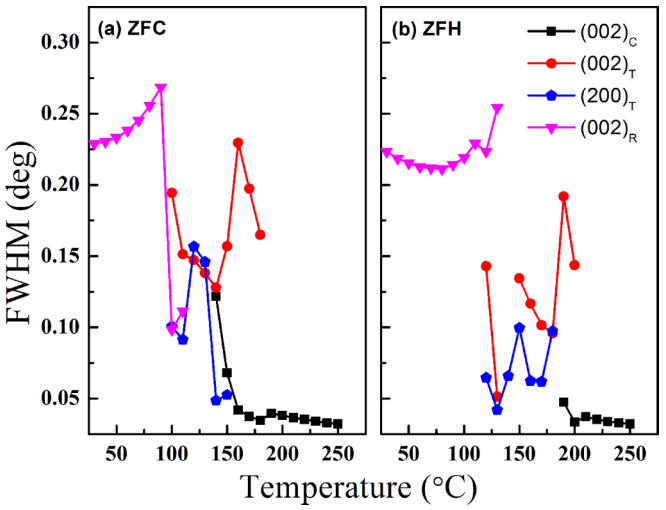

FIG. 5. (Color online) Temperature dependence of FWHM of various diffraction peaks along $(002)_C$ observed in Fig. 4 for (a) ZFC and (b) ZFH conditions.

The lattice parameters were then calculated from the diffraction peaks and are given in Fig. 6 over the entire temperature range studied. The phase transformation sequence in the ZFC and ZFH conditions is also labeled in this figure. The rhombohedral lattice parameters and the tilt angle (α) were obtained, cross-checked with the $(002)_R$ diffraction, and fitted to the (220) diffraction of the $(220)_R - (\bar{2}20)_R$ peaks. The tetragonal lattice parameters were also extracted from the $(002)_T$-$(200)_T$ doublet and cross-checked by the $(202)_T$ peak.

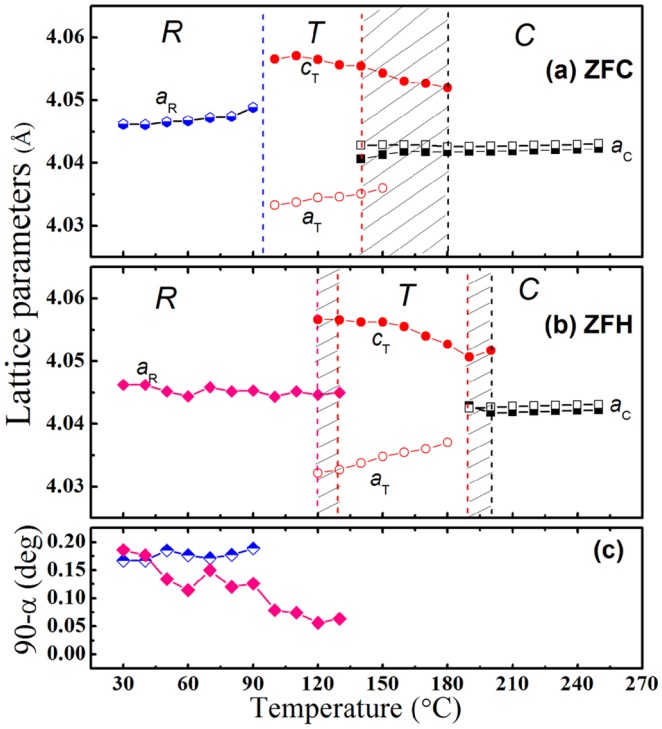

FIG. 6. (Color online) Lattice parameters as a function of temperature for (a) ZFC and (b) ZFH processes and (c) the tilt angles for R phase. The phase transition sequences for the two processes were also labeled in this figure. In the cubic region, the solid squares are obtained from the $(002)_C$ diffraction data, while the open squares are obtained from $(220)_C$ one. The shadow region indicated the coexistence of adjacent two phases. Solid lines drawn though the data points are for guides to the eyes.

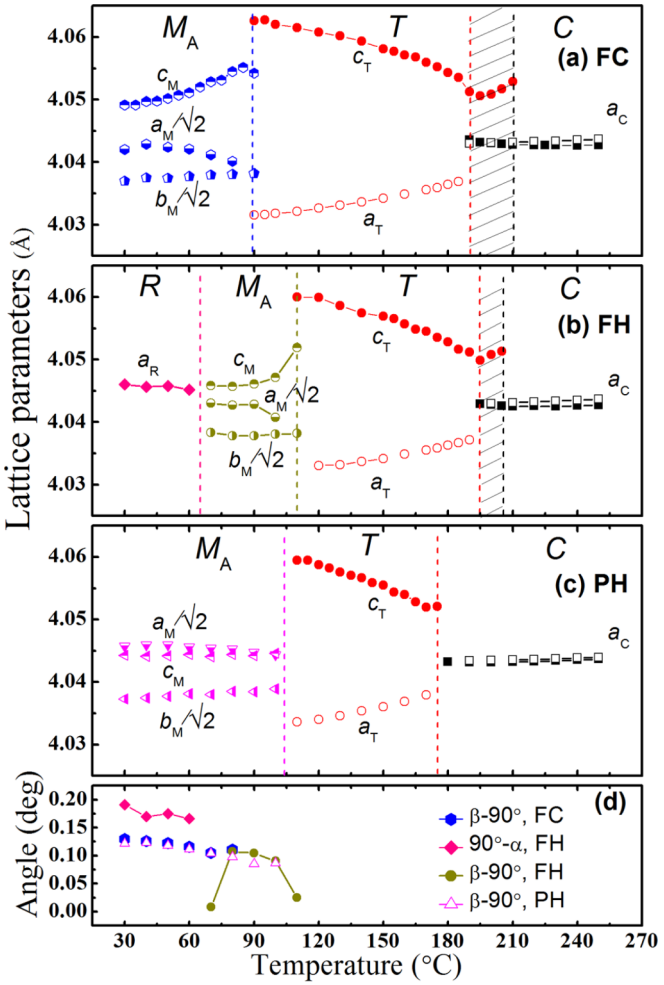

FIG. 7. (Color online) Temperature-dependent lattice parameters under (a) FC, (b) FH with $E = 1$ kV/cm, and (c) PH process. The tilting angles are presented in (d) of this figure. In the cubic phase region, the solid squares are obtained from the $(002)_C$ diffraction data, while the open squares are obtained from $(200)_C$ one. Solid lines drawn though the data points are for guides to the eyes.

The $(220)_T$ peak was not observed, which is quite common in single crystal diffraction measurements [43].

From the temperature evolution of the diffraction peaks (Fig. 4) and lattice parameters (Fig. 6), it can be seen that the $R \rightarrow T$ transition has a large thermal hysteresis of about 30 °C in zero-field. By contrast, the $C \rightarrow T$ zero-field transition is only about 10 °C. These thermal hysteresis regions are consistent with those observed in the dielectric data (see Fig. 3). The thermal hysteresis at the $R \rightarrow T$ boundaries may arise from a delay in the nucleation of the T-phase regions within the R matrix (on heating) relative to that of the R-phase regions within the T matrix (on cooling) and, correspondingly, the nucleation of the C phase regions within the T matrix (on heating) relative to that of the T phase regions within the C matrix (on cooling). These phase transitions, accompanied with hysteresis, indicate a first-order character of the phase transitions.

Insights into the larger thermal hysteresis of the $T \rightarrow C$ boundary may be obtained by comparing the lattice parameter data (Fig. 6) with that of the ZFC and ZFH dielectric data (Fig. 3). Interestingly, the ZFC and ZFH dielectric data, although having similar characteristics and values near room temperature and near the dielectric maximum, have notable different values between 75 and 150 °C. The ZFC data display a broad featureless dielectric profile on cooling below 150 °C; by contrast, the ZFH data exhibit a secondary shoulder near 125 °C, where the value of the dielectric constant is greater than that of the ZFC below this temperature and smaller above it. The comparisons of the ZFC and ZFH data indicate significant changes in the degree of PNDs self-organization into domain hierarchies with time at lower temperatures, which may be driven by elastic strain accommodation. The larger thermal hysteresis near the $T \rightarrow C$ boundary may then reflect that the ensemble of PNDs is less elastically relaxed.

C. FC, FH, and PH x-ray data

To clarify the field and temperature effects on the phase transformational sequence summarized in Fig. 2 and to obtain a better understanding of the PIN-PMN-PT structure-property relations for the various conditions, x-ray diffraction line scans were taken about the (002), (200), and (220) zones under $E =$ 0.5, 1, and 2 kV/cm for both the FC and FH conditions and under $E = 0$ kV/cm for the PH one. In addition, RMS were obtained about (200) and (220) at 150, 120, and 90 °C for the FC condition with $E = 1$ kV/cm; at 60, 90, and 120 °C for the

FH condition with $E = 1$ kV/cm; and at 30 and 130 °C for the PH condition with $E = 0$ kV/cm. The lattice parameters for the FC and FH conditions ($E = 1$ kV/cm) and for PH condition ($E = 0$ kV/cm) are given in Fig. 7.

1. FC ($E = 1$ kV/cm)

Above 210 °C for $E = 1$ kV/cm, the (002), (200), and (220) diffraction peaks do not exhibit any peak splitting, and it was found that the d spacing extracted from the (002) Bragg peak was equal to that from the (200), i.e., $c = a$ (experimental error is less around 0.001 Å). Thus, the stable phase is clearly C. On cooling to 210 °C, the c domain of the T phase became apparent in the cubic matrix, but the a domain was not detected until a lower temperature of 190 °C. Analogous behavior was found in the ZFC condition [see Figs. 4(a) and 6(a)]. However, the range of C and T phase coexistence was narrower relative to the ZFC condition [see Fig. 7(a)]. The signature of the T phase became more pronounced with decreasing temperature: the $(002)_T$ reflection peak shifted towards lower 2θ values, whereas the $(200)_T$ moved towards higher ones. These findings demonstrate that the lattice parameter c_T elongates and a_T contracts, as can be seen in Fig. 6(a). The RMS at 150 and 120 °C also verified that the T-phase symmetry was stable, where a single domain was observed around the (200) and (220) reflections. Although the (220) peak was narrow, a small shoulder was apparent at negative L values (see Fig. 8), which probably resulted from the crystal mosaic.

On decrease of the temperature to 90 °C, the monoclinic M_A phase was found to appear, which remained present on further cooling. As shown in Figs. 8(e) and 8(f), the pseudocubic (220) reflection exhibited the characteristic triple splitting of the M_A phase, which consisted of a $(040)_{MA}$ b domain and two twinned $(400)_{MA} - (\bar{4}00)_{MA}$ a domains, whereas the pseudocubic (200) exhibited the characteristic doublet splitting consisting of two twinned $(220)_{MA} - (\bar{2}20)_{MA}$ domains. The symmetric splitting along the transverse direction of the two a domains corresponds to the twin angle between the domains [6]. Thus the L coordinate value corresponds to a monoclinic angle of $\beta = 90.25°$, whose value was found to slightly increase with decrease of temperature [see Fig. 7(d)]. The M_A lattice parameters (c_M, b_M, and a_M) were respectively calculated from the $(002)_M c$ domain, $(040)_M b$ domain, and $(400)_M a$ domain, as shown in Fig. 7(a). It can clearly be seen that the value c_M exhibited a sharp decrease relative to c_T and then gradually decreased further with a decrease of temperature, whereas the values of $b_M/\sqrt{2}$ and $a_M/\sqrt{2}$ abruptly increased relative to a_T and were nearly independent of temperature on further decrease of temperature. These findings are unlike those for the $T \rightarrow M_A$ transition of binary PMN-PT crystals and PZT ceramics, where the values of $b_M/\sqrt{2}$ and a_T were reported to continuously decrease with decrease of temperature [11,43,44].

No evidence of M_C domain configurations in the FC condition were found in our structural investigations, analogous to those previously reported for PMN-x PT crystals with $x \leq 28$ [11]. Both line and mesh scans unambiguously indicated that the phase transformational sequence was $C \rightarrow T \rightarrow M_A$ for the FC condition with $E = 1$ kv/cm in our studies of PIN-PMN-PT crystals that exhibited a stable R phase in the initially annealed state. This phase sequence demonstrates that the MPB of this system bends over at higher temperatures, consistent with previous studies of binary ones. It is worth noting that x-ray diffraction revealed that the $C \rightarrow T$ boundary was shifted to higher temperature with increasing E, consistent with dielectric measurement (see Fig. 3). Interestingly, phase coexistence was found near the boundaries in the ternary systems, which increased with increase of E [45].

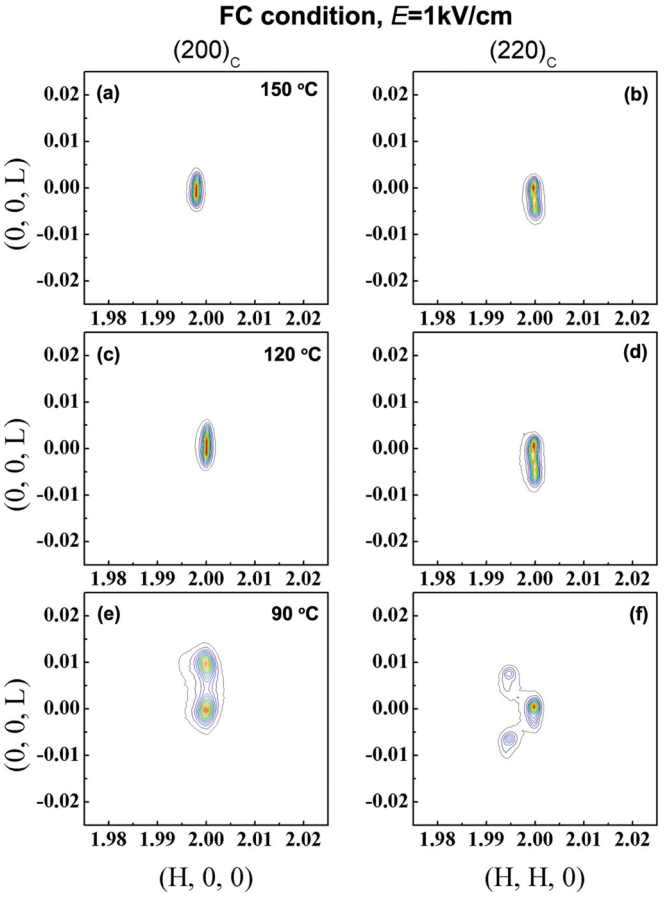

FIG. 8. (Color online) Reciprocal-space mesh scan around pseudocubic (200) and (220) zone at different temperature in FC process with $E = 1$ kV/cm parallel to [001] direction.

2. FH ($E = 1$ kV/cm)

We also studied the E dependence of the lattice parameters [shown in Fig. 7(b)] and phase transformational sequence on field heating from an initially annealed state. The results provide conclusive evidence of a $R \rightarrow M_A \rightarrow T \rightarrow C$ sequence in the FH condition. We summarize below our observation of the mesh and line (data not shown) scans.

(i) In the temperature range between 30 and 60 °C with $E = 1$ kV/cm, the PIN-PMN-PT crystal remained in a stable R phase. A broad single peak was observed around $(002)_C$ and $(200)_C$, while the pseudocubic (220) split into a $(220)_R - (\bar{2}20)_R$ doublet. This was verified by mesh scans, as shown in Figs. 9(a) and 9(b). The lattice parameter a_R and tilt angle α were extracted by fitting the (220) with a double Gaussian function, whose results agreed well with values determined from the (002), as shown in Figs. 7(b) and 7(d).

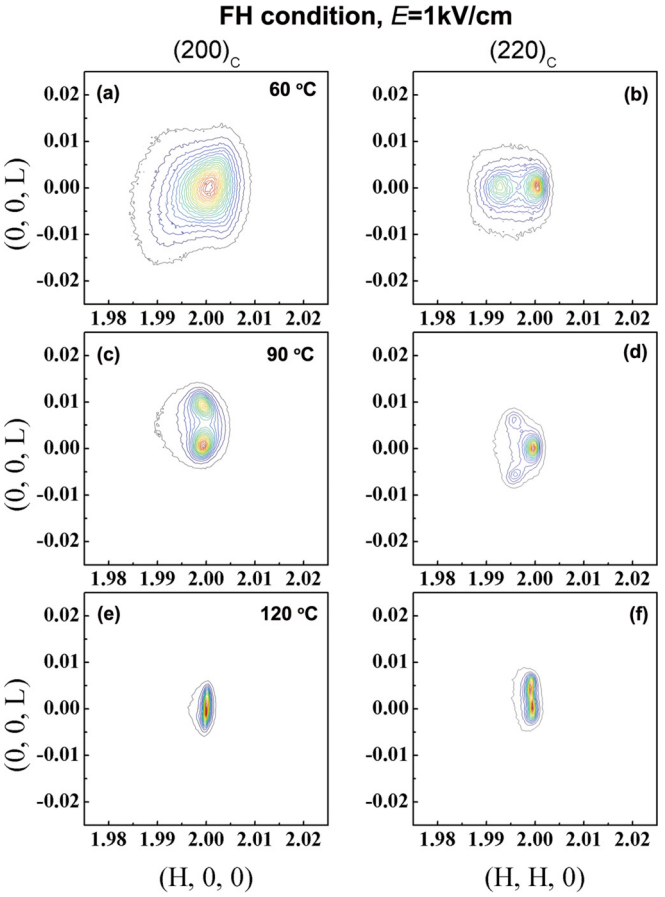

FIG. 9. (Color online) Reciprocal-space mesh scan around pseudocubic (200) and (220) zone at different temperature in FH process with $E = 1$ kV/cm parallel to [001] direction.

(ii) On heating to 70 °C, the signature M_A domain configurations were found in the mesh scans [see Figs. 9(c) and 9(d) at 90 °C, for example], i.e., a triplet splitting about (200) and a double about (220). The signature M_A mesh scans remained present over the temperature range of 70 to 110 °C.

(iii) With increasing temperature, a T phase was found to be stable. As can be seen from Figs. 9(e) and 9(f), mesh scans show a single domain about (200), revealing that the c domain was completely aligned along [001] under field. The tetragonal lattice parameters (c_T and a_T) were then extracted from (002) and (200) reflections, whose values were confirmed by measurements about the (220) reflection. The lattice parameters also exhibited a discontinuous change at the $M_A \rightarrow T$ transition in the FH condition [Fig. 7(b)], similar to those in the FC.

(iv) On heating to 190 °C, a $T \rightarrow C$ transition was found. Mesh scans (data not shown) revealed that the $(200)_T$ peak disappears and that the $(002)_C$ appeared. With further increase of temperature, the c domain of the T phase was attenuated, and a single sharp peak about (002) was found, which was similar to that in Fig. 4(c).

3. PH

As previously reported for poled rhombohedral binary PMN-PT and PZN-4.5PT crystals [13,16,18], the R phase was irreversibly transformed to M_A [see mesh scans in Figs. 10(a) and 10(b)]. With increase of temperature to 100 °C, signature reflection profiles of the T phase were observed. Compared to the T phase in the FC condition, most of the a domains were switched parallel to E in the PH state, however, some residual a domain peaks were found (data not shown). Lattice parameters extracted from the pseudocubic (002) and (200) were in good agreement. The mosaic of the crystal in the T phase was observed to be more significant in the PH condition, relative to either the FC or FH ones. This indicates that the domain state that is tuned by E tends to break down in the T phase of the PH condition. Note that in the PH condition, the value of c_M was close to $a_M/\sqrt{2}$, which was notably different from the corresponding values in the FC and FH ones. This may correspond to the singular case of a M_A cell, whose polarization vector lies very close to the rhombohedral polar axis [111] [see Fig. 2(b)] [13].

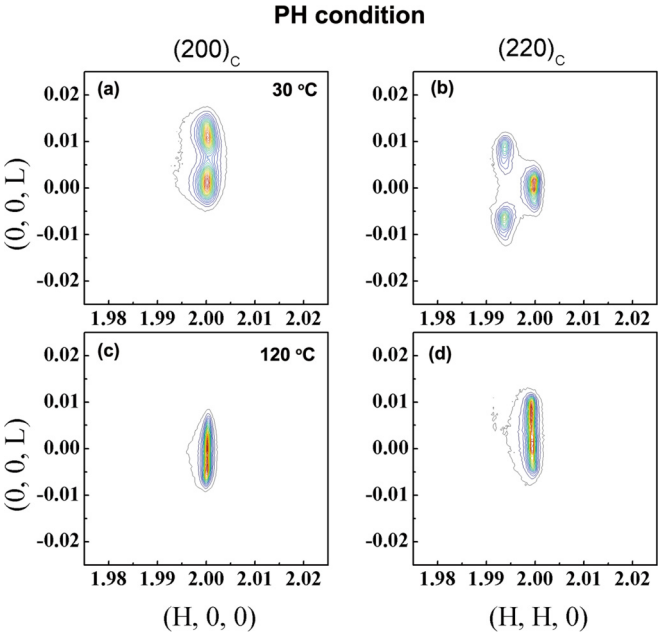

FIG. 10. (Color online) Reciprocal-space mesh scan around pseudocubic (200) and (220) zone at different temperature in PH process after specimen being poled along [001] direction.

D. Increasing field at fixed temperatures

Since the phase transformational sequence is dependent not only on the electrical and thermal histories, but also on the application sequence [15,16], we have also studied the phase stability at fixed temperatures (60 and 100 °C) with increasing E. Fields as high as 15 kV/cm were achieved along the thickness direction, but arching limited the field to $E =$ 8 kV/cm when applied along the side faces of the crystals.

Figures 11(a) and 11(b) show (002) line scans taken at 60 and 100 °C for E//[001]. It can be seen that the peaks shifted towards lower 2θ values with increasing E and then shifted to higher 2θ with subsequent decreasing E. Initially for $E = 0$ kV/cm, a single broad peak and a doublet splitting were observed along the pseudocubic (002) and (220) (data not shown) reflections at both 60 and 100 °C, respectively.

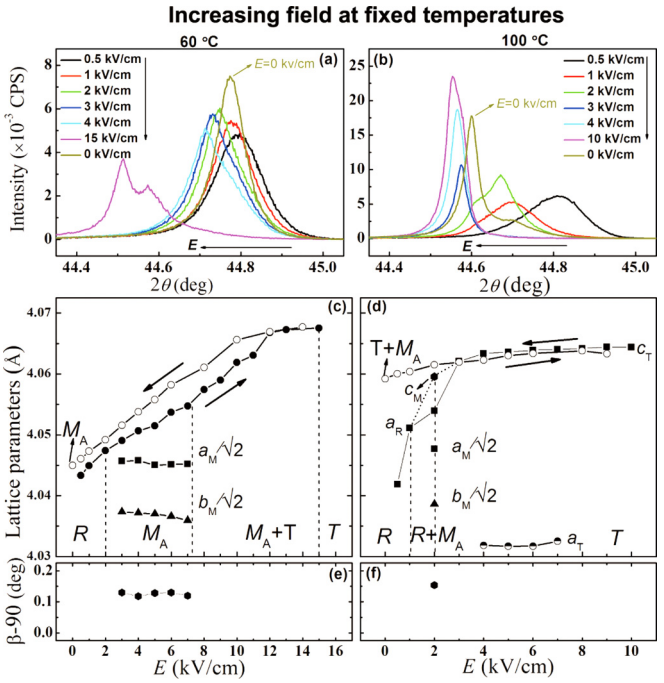

FIG. 11. (Color online) E-field evolution of pseudocubic (002) reflection peaks in an E-field circle with initially increasing from $E = 0$ kV/cm to $E = 15$ kV/cm or 10 kV/cm and then decreasing to $E = 0$ kV/cm at fixed temperature of (a) 60 °C and (b) 100 °C. The lattice parameters and the E-field-induced phase transition sequence were presented in the bottom panels: (c) at 60 °C and (d) at 100 °C.

The lattice parameters calculated from these reflections were consistent with a R phase. At 60 °C and for $E \geqslant 3$ kV/cm, a $R \rightarrow M_A$ transition occurred, as evidenced by the steady decrease of $a_M/\sqrt{2}$ and $b_M/\sqrt{2}$ and by the corresponding increase of c_m [see Figs. 11(c) and 11(e)]. With increasing E, the single peak about (002) became broader and asymmetric, indicating a gradual $M_A \rightarrow T$ transition, as predicted by polarization rotation theory [5]. A tetragonal single phase was not achieved for $E \leq 15$ kV/cm [see Fig. 11(a)]. An interesting feature of the data was that lattice parameter versus field response was quite anhysteretic with regards to the area between increasing and degreasing field lines. The main difference with the decreasing field data was that the initial R phase was not recovered, rather the M_A phase remained stable for $E = 0$ kV/cm. Unambiguously, the phase transformational sequence at 60 °C with increasing E, beginning from an initially annealed condition, was $R \rightarrow M_A \rightarrow T \rightarrow M_A$, as is labeled in Fig. 11(c).

At 100 °C in the initial annealed state, the stable phase was again R. With application of $E = 2$ kV/cm, coexisting R and M_A phases were found, as evidenced by a splitting of the

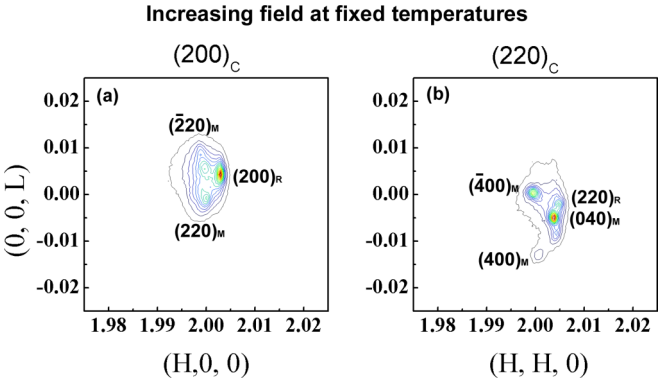

FIG. 12. (Color online) Reciprocal-space mesh scan around pseudocubic (200) and (220) zone with increasing E field to $E = 2$ kV/cm at fixed temperature of 100 °C.

(002) reflection along the longitudinal scan [see Fig. 11(b)] and by complexity in the mesh scan (see Fig. 12). From the $(002)_R$ and $(220)_R$ peaks, the R lattice parameter was calculated, as given in Fig. 11(d). A characteristic monoclinic triplet splitting was found about the pseudocubic (220) zone: a b_M domain identified by $(040)_M$, and a pair of a_M domains split along the transverse direction by $\beta = 90.15°$. For $E \geq 3$ kV/cm, a tetragonal single phase was induced. With subsequent decreasing E, the tetragonal (002) peaks gradually shifted to higher 2θ values and decreased in intensity. On further decrease of the field to $E \leq 3$ kV/cm, a low intensity M_A (002) reflection appeared with low intensity [see Fig. 11(b) for $E = 0$ kv/cm]. These data demonstrate that the M_A and T phase coexist on decreasing field for $E \leq 3$ kV/cm.

IV. CONCLUSIONS

Systematic x-ray diffraction studies of field and temperature effects on [001]-oriented rhombohedral PIN-PMN-PT crystals have been performed. The phase transformational sequence and phase stabilities have been summarized by constructing field-temperature phase diagrams for various histories. In the zero-field state, a phase sequence of $C \rightarrow T \rightarrow R$ is observed on cooling, and the reverse sequence of $R \rightarrow T \rightarrow C$ is found on heating. In the FC condition, the R phase is replaced by a monoclinic M_A phase, resulting in the sequence $C \rightarrow T \rightarrow M_A$. Field heating a previously ZFC crystal results in the sequence $R \rightarrow M_A \rightarrow T \rightarrow C$. The M_A phase is found to be stable after poling along [001], where the polarization vector is located close to rhombohedral [111] axis.

ACKNOWEDGMENT

This work was sponsored by the Office of Naval Research (No. N00014-13-1-0049).

[1] R. F. Service, Science **275**, 1878 (1997).
[2] S. E. Park and T. R. Shrout, J. Appl. Phys. **82**, 1804 (1997).
[3] M. Ahart, M. Somayazulu, R. E. Cohen, P. Ganesh, P. Dera, H.-K. Mao, R. J. Hemley, Y. Ren, P. Liermann, and Z. Wu, Nature **451**, 545 (2008).
[4] B. Noheda, D. E. Cox, G. Shirane, J. A. Gonzalo, L. E. Cross, and S. E. Park, Appl. Phys. Lett. **74**, 2059 (1999).
[5] H. X. Fu and R. E. Cohen, Nature **403**, 281 (2000).
[6] B. Noheda, D. E. Cox, G. Shirane, S. E. Park, L. E. Cross, and Z. Zhong, Phys. Rev. Lett. **86**, 3891 (2001).

[7] D. Vanderbilt and M. H. Cohen, Phys. Rev. B **63**, 094108 (2001).
[8] Y. M. Jin, Y. U. Wang, A. G. Khachaturyan, J. F. Li, and D. Viehland, Phys. Rev. Lett. **91**, 197601 (2003).
[9] Y. U. Wang, Phys. Rev. B **73**, 014113 (2006).
[10] H. Cao, F. M. Bai, N. G. Wang, J. F. Li, D. Viehland, G. Y. Xu, and G. Shirane, Phys. Rev. B **72**, 064104 (2005).
[11] H. Cao, J. F. Li, D. Viehland, and G. Y. Xu, Phys. Rev. B **73**, 184110 (2006).
[12] J. Yao, H. Cao, W. Ge, J. Li, and D. Viehland, Appl. Phys. Lett. **95**, 052905 (2009).
[13] B. Noheda, Z. Zhong, D. E. Cox, G. Shirane, S. E. Park, and P. Rehrig, Phys. Rev. B **65**, 224101 (2002).
[14] K. Ohwada, K. Hirota, P. W. Rehrig, P. M. Gehring, B. Noheda, Y. Fujii, S. E. E. Park, and G. Shirane, J. Phys. Soc. Jpn. **70**, 2778 (2001).
[15] K. Ohwada, K. Hirota, P. W. Rehrig, Y. Fujii, and G. Shirane, Phys. Rev. B **67**, 094111 (2003).
[16] F. M. Bai, N. G. Wang, J. F. Li, D. Viehland, P. M. Gehring, G. Y. Xu, and G. Shirane, J. Appl. Phys. **96**, 1620 (2004).
[17] H. Cao, J.-f. Li, and D. Viehland, J. Appl. Phys. **100**, 084102 (2006).
[18] M. Davis, D. Damjanovic, and N. Setter, Phys. Rev. B **73**, 014115 (2006).
[19] D. Viehland and J. F. Li, J. Appl. Phys. **92**, 7690 (2002).
[20] Y. Lu, D. Y. Jeong, Z. Y. Cheng, Q. M. Zhang, H. S. Luo, Z. W. Yin, and D. Viehland, Appl. Phys. Lett. **78**, 3109 (2001).
[21] S. Zhang and F. Li, J. Appl. Phys. **111**, 031301 (2012).
[22] L. Luo, W. Li, Y. Zhu, and J. Wang, Solid State Commun. **149**, 978 (2009).
[23] S. Zhang, J. Luo, W. Hackenberger, and T. R. Shrout, J. Appl. Phys. **104**, 064106 (2008).
[24] Y. Zhang, D. a. Liu, Q. Zhang, W. Wang, B. Ren, X. Zhao, and H. Luo, J. Electron. Mater. **40**, 92 (2011).
[25] Y. Zhang, X. Li, D. Liu, Q. Zhang, W. Wang, B. Ren, D. Lin, X. Zhao, and H. Luo, J. Cryst. Growth **318**, 890 (2011).
[26] F. Li, S. Zhang, Z. Xu, X. Wei, J. Luo, and T. R. Shrout, J. Appl. Phys. **107**, 054107 (2010).
[27] P. Finkel, H. Robinson, J. Stace, and A. Amin, Appl. Phys. Lett. **97**, 122903 (2010).
[28] P. Finkel, K. Benjamin, and A. Amin, Appl. Phys. Lett. **98**, 192902 (2011).
[29] P. Zhao, S. Goljahi, W. Dong, T. Wu, P. Finkel, R. Sahul, K. Snook, J. Luo, W. Hackenberger, and C. S. Lynch, Smart Materials and Structures **20**, 055006 (2011).
[30] P. Finkel, A. Amin, S. Lofland, J. Yao, and D. Viehland, Phys. Status Solidi A and Materials Science **209**, 2108 (2012).
[31] S. Zhang, F. Li, J. Luo, R. Xia, W. Hackenberger, and T. R. Shrout, Appl. Phys. Lett. **97**, 132903 (2010).
[32] X. Li, Y. Wang, L. Liu, X. Zhao, H. Luo, and D. Lin, Materials Chemistry and Physics **122**, 350 (2010).
[33] G. Xu, P. M. Gehring, C. Stock, and K. Conlon, Phase Transitions **79**, 135 (2006).
[34] G. Y. Xu, H. Hiraka, G. Shirane, and K. Ohwada, Appl. Phys. Lett. **84**, 3975 (2004).
[35] G. Y. Xu, Z. Zhong, Y. Bing, Z.-G. Ye, C. Stock, and G. Shirane, Phys. Rev. B **67**, 104102 (2003).
[36] P. M. Gehring, W. Chen, Z. G. Ye, and G. Shirane, J. Phys. Condens. Matter **16**, 7113 (2004).
[37] G. Y. Xu, D. Viehland, J. F. Li, P. M. Gehring, and G. Shirane, Phys. Rev. B **68**, 212410 (2003).
[38] V. Westphal, W. Kleemann, and M. D. Glinchuk, Phys. Rev. Lett. **68**, 847 (1992).
[39] H. Cao, F. M. Bai, J. F. Li, D. Viehland, G. Y. Xu, H. Hiraka, and G. Shirane, J. Appl. Phys. **97**, 094101 (2005).
[40] P. M. Gehring, K. Ohwada, and G. Shirane, Phys. Rev. B **70**, 014110 (2004).
[41] B. E. Vugmeister and M. D. Glinchuk, Rev. Mod. Phys. **62**, 993 (1990).
[42] D. Phelan, C. Stock, J. A. Rodriguez-Rivera, S. Chi, J. Leao, X. Long, Y. Xie, A. A. Bokov, Z.-G. Ye, P. Ganesh, and P. M. Gehring, Proc. Nat. Acad. Sci. USA **111**, 1754 (2014).
[43] H. Cao, J. Li, and D. Viehland, J. Appl. Phys. **100**, 034110 (2006).
[44] B. Noheda, J. A. Gonzalo, L. E. Cross, R. Guo, S. E. Park, D. E. Cox, and G. Shirane, Phys. Rev. B **61**, 8687 (2000).
[45] C. Luo, Y. Wang, Z. Wang, W. Ge, J. F. Li, D. Viehland, and H. Luo (unpublished).